

Recurrent neural network analysis of single trajectories switching between anomalous diffusion states

Alvaro Lanza

Department of Physics, King's College London, WC2R 2LS, United Kingdom

Xiang Qu

Department of Physics, King's College London, WC2R 2LS, United Kingdom

Stefano Bo

Department of Physics, King's College London, WC2R 2LS, United Kingdom

E-mail: stefano.bo@kcl.ac.uk

Abstract. Diffusive dynamics abound in nature and have been especially studied in physical, biological, and financial systems. These dynamics are characterised by a linear growth of the mean squared displacement (MSD) with time. Often, the conditions that give rise to simple diffusion are violated, and many systems, such as biomolecules inside cells, microswimmers, or particles in turbulent flows, undergo anomalous diffusion, featuring an MSD that grows following a power law with an exponent α . Precisely determining this exponent and the generalised diffusion coefficient provides valuable information on the systems under consideration, but it is a very challenging task when only a few short trajectories are available, which is common in non-equilibrium and living systems. Estimating the exponent becomes overwhelmingly difficult when the diffusive dynamics switches between different behaviours, characterised by different exponents α or diffusion coefficients K . We develop a method based on recurrent neural networks that successfully estimates the anomalous diffusion exponents and generalised diffusion coefficients of individual trajectories that switch between multiple diffusive states. Our method returns the α and K as a function of time and identifies the times at which the dynamics switches between different behaviours. We showcase the method's capabilities on the dataset of the 2024 Anomalous Diffusion Challenge.

1. Introduction

Diffusive processes govern life at the microscale [1]. Einstein provided the mathematical description for diffusion relying on the assumption that the observed increments are unbiased, statistically independent, of finite size, and stationary [2, 3]. This formalism conveniently models many systems in physics, biology, ecology and finance [4]. The hallmark of diffusion is a linear growth of the mean squared displacement (MSD) with time, which can be seen as a consequence of the central limit theorem [5–7]. For a system described by a variable $\mathbf{X}(t)$, we define $\text{MSD}(t) \equiv \text{E}[|\mathbf{X}(t) - \mathbf{X}(0)|^2]$ where $\text{E}[\cdot]$ denotes the ensemble average. The mentioned linear increase is

$$\text{MSD}(t) = 2dDt, \quad (1)$$

where d is the spatial dimensionality of the system and D is the diffusion coefficient. Einstein’s description of diffusion was fundamental in demonstrating that matter is made of atoms by observing their indirect effects on the motion of a tracer [3]. His efforts to learn the physical properties of a system by observing the statistics of a tracer immersed in it were later developed into what became the field of microrheology [8]. Einstein’s assumptions for diffusive processes are very well satisfied for dilute suspensions as the pollen grains observed by Robert Brown [9] and for the motion of colloids in water, free or confined by optical tweezers [10, 11]. However, these assumptions are violated in crowded nonequilibrium environments such as the cell interior, in the motion of microswimmers, and in many active matter and turbulent systems. If any of the assumptions is violated, under general conditions [6, 12–14], the mean squared displacement grows with a power-law

$$\text{MSD}(t) \propto Kt^\alpha, \quad (2)$$

where α is the anomalous diffusion exponent and K is the generalised diffusion coefficient with dimension $[\text{length}^2 \text{time}^{-\alpha}]$ [15–18]. The exponent α discriminates between normal diffusion ($\alpha = 1$) and anomalous diffusion ($0 < \alpha < 1$ for sub-diffusion, and $1 < \alpha < 2$ for super-diffusion). Determining the anomalous exponent α and the generalised diffusion coefficient K provides crucial information on the system being studied and sheds light on the physical processes at play, which are not directly observable, as, for example, in studies of chromatin dynamics and genome search processes [19–23]. It is also of great importance to detect changes in diffusive states and to determine the time at which they occur. Unfortunately, in most systems of interest, it is challenging to experimentally obtain many trajectories under the same conditions [24], which makes it difficult to apply methods relying on ensemble averages such as [13, 25–35]. This difficulty motivated the development of methods which work on an individual trajectory level [31, 32, 35–44]), which, however, struggle when only short trajectories are available, a commonplace scenario in non-equilibrium and biophysical experiments. The importance of inferring the anomalous exponent and the generalised diffusion coefficient, combined with difficulty of the task, called for the development of machine-learning approaches (see, *e.g.*, [45–69]), with recent studies developing methods that learn to generate stochastic processes

that closely resemble anomalous diffusion ones [70]. In 2020, the Anomalous Diffusion Challenge (AnDi) gathered the community to identify the best methods for analysing anomalous diffusion from single trajectories [71]. Machine-learning approaches proved to be the best-performing ones on single trajectories, a trend confirmed also by the 2024 Anomalous Diffusion Challenge (AnDi2024) [72, 73], which we will discuss in detail below.

Inspired by AnDi2024, in this contribution, we tackle the challenging task of inferring the anomalous diffusion exponent α and generalised diffusion coefficient K from a short single trajectory that displays multiple transitions between different diffusive states, characterised by different α and K [72]. Building on previous work [46, 57, 74] we develop a method based on recurrent neural networks employing Long Short-Term Memory architectures (LSTM) [75, 76]. Following the approach of Ref. [60], our method returns a prediction of α and K as a function of time. We also develop a neural network to detect changes between diffusive states and identify the time at which it occurred, *i.e.* the changepoint (CP). We also discuss the possibility of inferring a CP from the time-dependent estimate of $\hat{\alpha}(t)$ and $\hat{K}(t)$ using a state-of-the-art changepoint detection algorithm [77] and contrast the performances of this approach with those of a neural network designed to identify the changepoints. We name our method **sequandi**, benchmark its performances on the AnDi2024 dataset and make it freely available [78].

In the next paragraph, we briefly summarise the scope of The Anomalous Diffusion Challenge 2024 [72]. In Section 2, we outline the architecture and the training procedure of our method. Section 3 discusses the task of inferring the time-dependent evolution of the anomalous diffusion exponent α and the generalised diffusion coefficient K , while Section 4 focuses on finding the changepoints between different types of diffusive motion. Finally, in Section 5, we apply our method to the dataset of AnDi2024 and discuss its performance.

The Anomalous Diffusion Challenge 2024. The present work was motivated by the problems and data of The Anomalous Diffusion Challenge 2024 (AnDi2024) [72]. AnDi2024 is a challenge where multiple research groups competed to showcase the performances of their methods for the inference of the anomalous diffusion exponent α and generalised diffusion coefficient K from single short two-dimensional trajectories (featuring a number of time steps, T , between 20 and 200) from a common dataset[‡], as the one shown in Fig. 1. A notable difference from the first edition of the challenge [71] is that the trajectories can feature multiple transitions between different diffusive states. A segment between two transitions can be as short as 3 time steps. Establishing when such transitions occur, *i.e.*, identifying the changepoint (CP) times, t_i^{CP} , is one of the tasks of the challenge.

The AnDi2024 trajectories are generated based on five physical models of diffusion

[‡] Part of the challenge featured the analysis of microscopy videos and ensembles of trajectories, but we focus on the single-trajectory analysis.

undergoing fractional Brownian motion [72].

- *Single state*: fractional Brownian motion trajectories characterised by α and K without changepoints.
- *Multiple state*: trajectories switching between two or more different diffusive states, each characterised by their α and K .
- *Transient confinement*: trajectories switch between two different α and K states when the particles leave or enter spatially distributed compartments, a common biological scenario.
- *Dimerisation*: considers two particles that can dimerise and begin to co-diffuse or undimerise and resume independent diffusion. From the viewpoint of a single trajectory, this is also a two-state model with switching α and K .
- *Quenched trap*: trajectories switch between a free diffusion and a completely immobile state, which they transiently occupy upon encountering a trap.

The anomalous diffusion exponent α varies between 0 and 2: $0 < \alpha < 2$. The generalised diffusion coefficient K spans a broad range $10^{-12} \leq K \leq 10^6$. Except for the immobile state in the quenched trap model, in the other models there are no restrictions within these ranges on the allowed values of α and K between consecutive diffusive states. We report the performances of our method on a benchmark dataset similar to the one of AnDi2024 [79].

2. Neural network architecture and training procedure

2.1. Architecture.

We build our architecture on the one proposed in Ref. [57], which performed very well on the first AnDi Challenge [71]. As illustrated in Fig. 1, the network features two layers of Long Short-Term Memory (LSTM) cells [75, 76] enabling it to capture long and short-term correlations, while securing stability in the training [80]. An important feature of recurrent neural networks such as LSTMs is that they can receive as input a sequence of arbitrary length and return another sequence of the same length. This allows us to task the network to analyse trajectories of varying length and to return the time-dependent values of α and K along the trajectory, which is suitable to characterise conditions that frequently switch between different behaviours, as suggested in Ref. [60]. The first LSTM layer has dimension 250 and the second one 50. After the second LSTM layer, the sequence goes through a Time-Distributed layer [81]. This connects the sequence returned by the second LSTM to the output layer. Wishing to preserve the sequential output of the LSTM layers, Keras' TimeDistributed layer applies a fully connected layer for each block in the input sequence, which are processed independently with a shared weight, returning a 2D vector of length matching the input and of a width dependent on the inference task. This layer and the ability to return the time evolution of α and K are the main innovations to Ref. [57]. The shape of the output layer depends on the specific task, as we will discuss below.

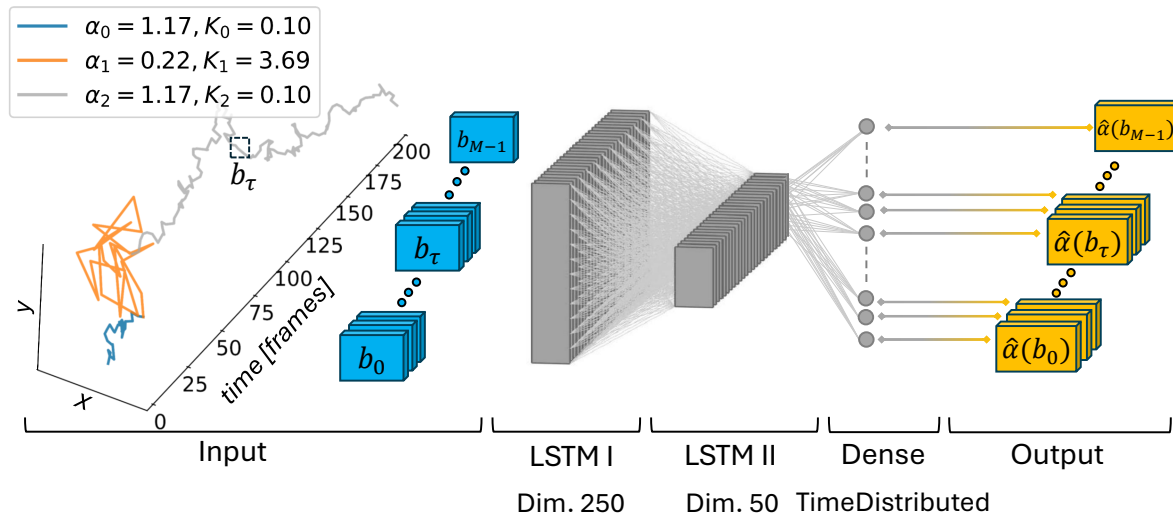


Figure 1. Neural Network Architecture of sequandi. 2D trajectory data is normalised and separated into M blocks b_τ of 3 coordinate increments each. The blocks are then fed into two adjacent long short-term memory (LSTM) layers of dimensions 250 and 50. Next, outputs from the second LSTM layer are passed through a dense TimeDistributed layer, which is adapted depending on the task (inference of α , K or t^{CP}) and returns a sequence of length M , ready for post-processing.

2.2. Pre-processing.

We train the networks on the increments between subsequent trajectory coordinates. For a trajectory of length T , this means $T - 1$ increments per each of the two spatial dimensions $\Delta x_t = x_{t+1} - x_t$ and $\Delta y_t = y_{t+1} - y_t$. When working with neural networks, it is customary to normalise the input data (see, *e.g.*, Ref. [46, 57, 74]). However, a normalisation of the increments with respect to their standard deviation or their maxima can obfuscate information about the generalised diffusion coefficient K . Therefore, in addition to a typical standardisation, normalising the Δx_t and Δy_t in each trajectory together so their combined mean is zero and variance is 1, we include their standard deviation σ in the input vector. When training LSTMs, it is often convenient for the training to group the input time series into blocks. The choice of an optimal block size results from several trade-offs. Since the AnDi2024 data features segments with a minimum length of 3, we choose a block to include 3 increments per spatial dimension. The input trajectory is then reshaped into M blocks of dimension 9\S ,

$$b_\tau = [\Delta x_{3\tau}, \Delta y_{3\tau}, \sigma, \Delta x_{3\tau+1}, \Delta y_{3\tau+1}, \sigma, \Delta x_{3\tau+2}, \Delta y_{3\tau+2}, \sigma] \quad (3)$$

where the subscript τ denotes the order in sequence of the blocks and $\tau = 0, \dots, M - 1$, as shown in Fig. 2. The total number of blocks M is equal to the $\lceil (T - 1)/3 \rceil$ ceiling division. Therefore, there may not be enough increments to fill the last block. All such “missing” increments are padded with a dummy value, which is later ignored by the network in a procedure known as masking.

\S Note that σ is added on after every coordinate in the block.

2.3. Training Procedure.

Andi2024 considered a wide range of model experiments. We therefore opted to use a training set which is mixed and contained an equal representation of each model experiment. This also opens the door to apply our network to generic diffusive trajectories, as our approach does not involve a prior screening to first ascertain the type of Challenge-specific diffusive model. We trained our network on simulated trajectories using the `andi-datasets` Python library provided by the challenge organisers [82]. When training a network to infer a parameter from an interval, there is often a tendency to underestimate the values close to the upper limit of the interval and overestimate the ones close to the lower limit, giving rise to an S-shaped curve when plotting predictions vs the ground truth (see, *e.g.*, [57]). To mitigate this issue, we slightly biased the training dataset to have more cases with α closer to the extremes of the supported $(0, 2)$ range [see Fig. A1(a)]. While the support for K is vast, $[10^{-12}, 10^6]$, we trained for $K < 35$. A high representation of $K \leq 1$ was considered as this regime is paradigmatic of confined states and has a higher relative importance in its evaluation with a logarithmic metric, discussed in the next section [see Fig. A1(b)]. Lastly, due to the nature of our CP detection method, we included sets of trajectories with many CP (that is, short segments). In total, we trained on 2.5×10^6 simulated trajectories.

We use a batch size of 32, and a cycling of the training data of 20 epochs, with an early stopping monitor to prevent overfitting. As common with LSTM training, we apply 20% recurrent dropout to both LSTM layers to prevent overtraining [57, 83], and 10% of the data is kept for validation. We use the Adam optimizer with learning rate $l_R = 10^{-3}$ and numerical stability constant $\epsilon = 10^{-7}$ [84].

The particular labelling and losses for the training procedures of α and K are discussed in Section 3 and, for t^{CP} , in Section 4.

LSTMs can analyse time series data of varying lengths, which is of great importance for experimental applications and for studying the AnDi2024 dataset, which contains trajectories of length between 20 and 200. However, for convenience, we train the network on batches where all input trajectories are modified to have the same length $T = 200$. As for the blocks, this modification is achieved by padding the missing values with a value, which is later ignored by a masking layer.

3. Inferring the time evolution of the anomalous exponent $\alpha(t)$ and generalised diffusion coefficient $K(t)$

In this Section, we focus on the task of inferring the time-dependent (point-wise) anomalous exponent α and generalised diffusion coefficient K . We refer to our estimates as $\hat{\alpha}(t)$ and $\hat{K}(t)$, while $\alpha(t)$ and $K(t)$ denote the ground truth. As in AnDi2024, we consider trajectories that switch between different α and K , so that the ground truth $\alpha(t)$ and $K(t)$ is a piecewise constant function of t , as shown by the blue curve in Fig. 3.

3.1. Loss function and last layer for inferring $\alpha(t)$ and $K(t)$

The architecture of the first two LSTM layers is the same for all networks we train. The last layer, instead, is tailored to the specific task. For the inference of $\alpha(t)$ and $K(t)$, the TimeDistributed output layer returns 2 floats for every block b_τ in the input sequence, yielding the block predictions $\hat{\alpha}(b_\tau)$ and $\hat{K}(b_\tau)$. The loss function for both parameters is a mean squared error (MSE) between the prediction and the ground truth. The ground truth of a block is defined as the time average of the $\alpha(t)$ and $K(t)$, respectively, within a block.||

3.2. Post processing

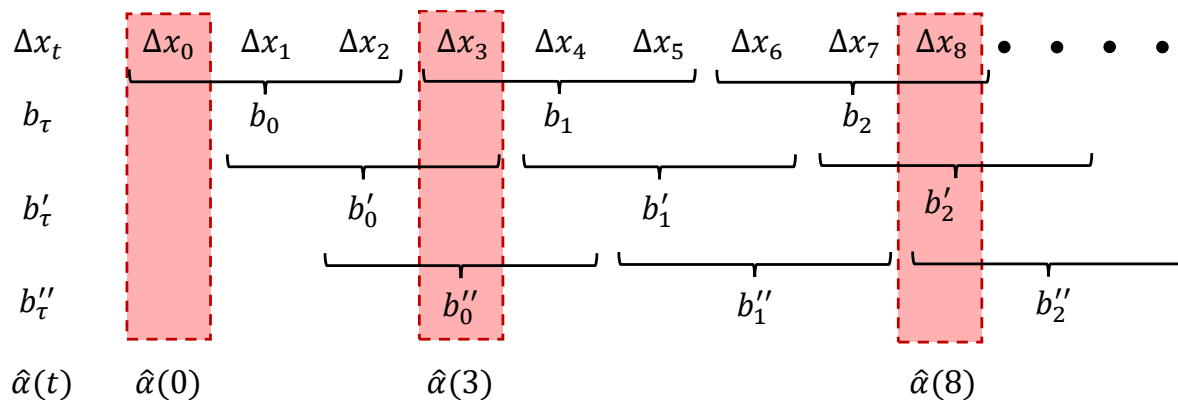


Figure 2. Block assignment and point-wise inference. The input trajectory is split into blocks b_τ containing three increments per spatial dimension as stated in Eq. (3). The network returns block-wise predictions $\hat{\alpha}(b_\tau), \hat{K}(b_\tau)$. To obtain a point-wise prediction, for each increment, we shift the trajectory by one and two increments, respectively, changing which increments are assigned to each block $b'_\tau = [\Delta x_{3\tau+1}, \Delta y_{3\tau+1}, \sigma, \Delta x_{3\tau+2}, \Delta y_{3\tau+2}, \sigma, \Delta x_{3\tau+3}, \Delta y_{3\tau+3}, \sigma]$, and $b''_\tau = [\Delta x_{3\tau+2}, \Delta y_{3\tau+2}, \sigma, \Delta x_{3\tau+3}, \Delta y_{3\tau+3}, \sigma, \Delta x_{3\tau+4}, \Delta y_{3\tau+4}, \sigma]$. This returns staggered predictions $\hat{\alpha}(b'_\tau), \hat{K}(b'_\tau), \hat{\alpha}(b''_\tau), \hat{K}(b''_\tau)$. We obtain the point-wise $\hat{\alpha}(t)$ and $\hat{K}(t)$ by averaging the block predictions of the blocks that contain the time t , illustrated by the shifting red square. For instance, consider the vertical slice corresponding to $t = 3$. The point-wise dynamical prediction is obtained as $\hat{\alpha}(t = 3) = [(\hat{\alpha}(b_1) + \hat{\alpha}(b'_0) + \hat{\alpha}(b''_0))]/3$. For $t = 0$ and 1, we only use $\hat{\alpha}(b_\tau)$ predictions from blocks $\tau = 0$ and $\tau = 0, 1$, respectively.

The block estimates $\hat{\alpha}(b_\tau)$ and $\hat{K}(b_\tau)$ are, in effect, coarse-grained predictions averaging three successive time increments. To build the refined point-wise $\hat{\alpha}(t)$ and $\hat{K}(t)$, we pool the predictions of 3 trajectories: the original trajectory, and the original trajectory shifted by one and two frames, respectively, as shown in Fig. 2.

|| For α (and similarly for K), the ground truth (label) of a block is $\alpha(b_\tau) = \frac{1}{3}[\alpha(t = 3\tau) + \alpha(t = 3\tau + 1) + \alpha(t = 3\tau + 2)]$, using fewer $\alpha(t)$ if a semi-padded block. This label is the mean of the α values corresponding to the increments of that particular block, allowing for a contribution from every $\alpha(t)$ in the case of a CP.

3.3. Diffusion inference performances

In Fig. 3, we plot an example from the trajectory illustrated in Fig. 1 of the point-wise sequential predictions. The generalised diffusion coefficient is plotted as $\log[K(t) + 1]$ [¶]. To assess the performance of our method, we compute the following metrics for the point-wise dynamic predictions $\hat{\alpha}(t)$ and $\hat{K}(t)$ in a given trajectory with $T-1$ increments

$$\text{MAE}_{\alpha(t)} = \frac{1}{T-1} \sum_{t=0}^{T-2} |\alpha(t) - \hat{\alpha}(t)|, \quad (4)$$

$$\text{MSLE}_{K(t)} = \frac{1}{T-1} \sum_{t=0}^{T-2} \left[\log[K(t) + 1] - \log[\hat{K}(t) + 1] \right]^2. \quad (5)$$

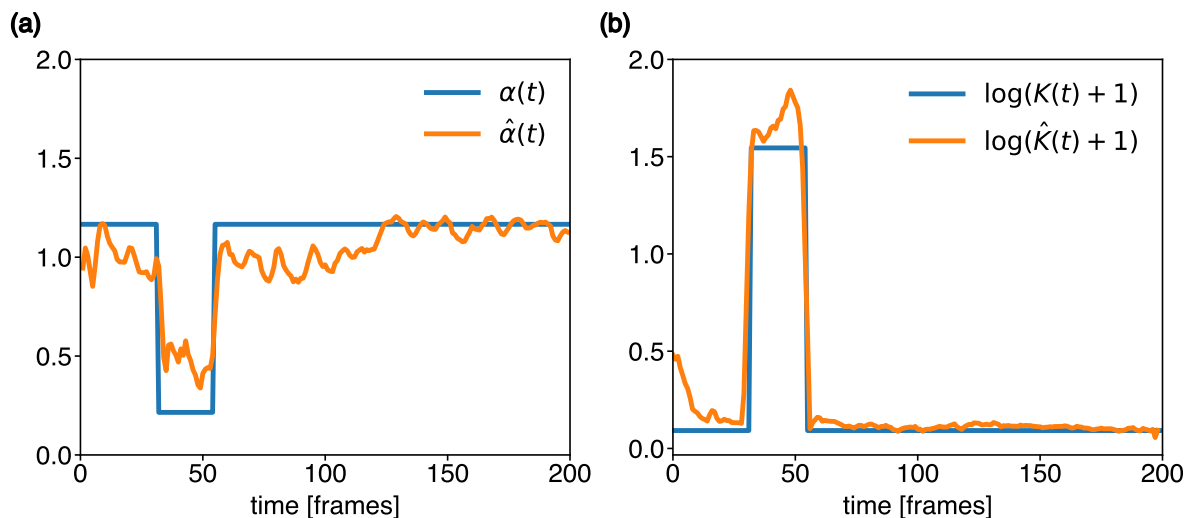


Figure 3. Example of $\hat{\alpha}(t)$ and $\hat{K}(t)$ and ground truth. Results from example trajectory in Fig. 1. **(a)** The orange line is `sequandi`'s point-wise prediction of the anomalous exponent $\hat{\alpha}(t)$, and the blue piece-wise constant line is the ground truth $\alpha(t)$. **(b)** The orange line is based on `sequandi`'s point-wise prediction of the generalised diffusion coefficient $\hat{K}(t)$, and is $\log(\hat{K}(t)+1)$. The blue piece-wise constant line is the ground truth $\log(K(t)+1)$. The prediction tracks the ground truth with an $\text{MAE}_{\alpha(t)} = 0.134$ and $\text{MSLE}_{K(t)} = 0.010$.

We measure these metrics for every trajectory in the benchmark dataset, and then take a mean over all the trajectories' errors. For this dataset, $\text{MAE}_{\alpha(t)} = 0.191$ and $\text{MSLE}_{K(t)} = 0.021$ ⁺. We discuss these performances in greater detail in Section 5.

[¶] This is the argument for the mean squared logarithmic error (MSLE) used to evaluate the performance in inferring K in AnDi2024 and ensures a linear-like loss for small K and a logarithmic one for large K .

⁺ The AnDi2024 metrics considered a flattened array of all t across all trajectories in the dataset instead of a per-trajectory average. Using this metric we obtain $\text{MAE}_{\alpha(t)} = 0.176$ and $\text{MSLE}_{K(t)} = 0.014$.

4. Identifying the changepoints

In this Section, we present our approach to detecting changes between diffusive states and inferring the time at which the changes took place. The trajectories we are considering often involve multiple changes and we denote by t_i^{CP} the time at which the i^{th} change in diffusion states occurred. We train a network specifically to detect and locate CPs. In Section 4.4, we discuss the alternative approach of inferring the CP with an algorithm that studies the changes in the $\hat{\alpha}(t)$ and $\hat{K}(t)$ predictions made in Section 3, as done, for example in Ref. [56].

4.1. Output layer for changepoint detection and location

To detect and locate changes in diffusive states, we compare the performances of two types of networks. One network is tasked to both infer the pointwise time-dependent evolution of $\alpha(t)$ and $K(t)$, and to detect and locate changepoints. Another network is only tasked to detect and locate the CPs, without explicitly inferring $\alpha(t)$ and $K(t)$. This second network, focusing only on the detection and location of CPs, provides the best performances.

The architecture of the network involves the two LSTM layers described in Section. 2, and a specific structure of the output TimeDistributed layer, which features *two* separate TimeDistributed layers, in parallel. One layer is for detection, the other for location, specifically tasked with the following:

- *Detection: Is there a CP in the block?* This is a binary classification task with an integer label $t_{I/O}^{\text{CP}}(b_\tau) = 0$ (in absence of CP) or 1 (in presence of CP). For this layer, we employ a standard binary cross-entropy loss function and sigmoid activation function. The model’s predictions are given in one number per block, the probability that there is a CP within it. We round this number with the default threshold of 0.5 to obtain $\hat{t}_{I/O}^{\text{CP}}(b_\tau) = 0$ or 1.
- *Location: where in the block is the CP?* Each block contains up to three different t where a CP may be located, so we train this parallel output to predict on labels $t_{loc}^{\text{CP}}(b_\tau) = 0, 1, 2$ or 3. The zero label is used when there is no CP in the block, and the non-zero labels indicate the position of the block where the ground truth CP is. It is important to retain information about the order of the CPs (*e.g.*, if a CP is at $t = 1$, predicting a CP at $t = 2$ is “less wrong” than predicting it at $t = 3$). We therefore choose the *ordinal* categorical cross-entropy OCE [85] as the loss function. This loss function takes into consideration the order of the number of classes ($L = 4$) by weighing the standard cross-entropy loss CE with the distance between predictions and ground truth

$$\text{OCE} (t_{loc}^{\text{CP}}(b_\tau), \hat{\mathbf{t}}_{loc}^{\text{CP}}(b_\tau)) = (w + 1) \text{CE} (t_{loc}^{\text{CP}}(b_\tau), \hat{\mathbf{t}}_{loc}^{\text{CP}}(b_\tau)), \quad (6)$$

$$w (t_{loc}^{\text{CP}}(b_\tau), \hat{\mathbf{t}}_{loc}^{\text{CP}}(b_\tau)) = \frac{|t_{loc}^{\text{CP}}(b_\tau) - \arg \max \hat{\mathbf{t}}_{loc}^{\text{CP}}(b_\tau)|}{L - 1}. \quad (7)$$

Note the predictions $\hat{\mathbf{t}}_{\text{loc}}^{\text{CP}}(b_\tau)$ are in a probability vector format (after having passed through a softmax activation function).^{*} Lastly, an argmax function is applied to $\hat{\mathbf{t}}_{\text{loc}}^{\text{CP}}(b_\tau)$ to predict the most likely location of the CP.

4.2. Post processing

As for the inference of $\alpha(t)$ and $K(t)$ discussed in Section 3, we pool the results from three versions of the same trajectory by shifting it by one and two increments (see Fig. 2). In this case, we have two types of signals for a CP from the two parallel final layers, one concerning the detection and one the location of the CP. Sometimes, these two outputs are inconsistent (*e.g.*, the detection layer may predict that there is no CP while the location layer may predict that a change occurred and at a specific time). Our pooling consists of summing the six outputs (2 outputs for each of the three shifted trajectories), which for non-zero predictions each provide one count at the time(s) they are indicating. The resulting $\hat{t}^{\text{CP}}(t)$ is a time-dependent curve peaking where the neural network consistently detects a CP, as shown in Fig. B1. We then search for all peaks that contain at least the threshold value of 2 counts (chosen to mitigate the risk of missing a CP, *i.e.*, a false negative) and assign the location of the peak as the CP prediction \hat{t}_i^{CP} . In Fig. 4, we report this prediction \hat{t}_i^{CP} as the solid vertical lines.

4.3. Changepoint detection and location performances

In the AnDi challenge, the Jaccard similarity coefficient JSC_{CP} is used as metric for the accuracy of detecting a CP. For a set of true positive (TP) detections[‡]

$$\text{JSC}_{\text{CP}} = \frac{\text{TP}}{\text{TP} + \text{FN} + \text{FP}}, \quad (8)$$

where FN denotes the number of false negatives, FP, the number of false positives, and $\text{JSC}_{\text{CP}} = 1$ for perfect detections. The algorithm used to identify these quantities from ground truth t_i^{CP} and predicted \hat{t}_j^{CP} relies on pairing segments i, j together by minimising the distance between them $d_{i,j} = \min(|t_i^{\text{CP}} - \hat{t}_j^{\text{CP}}|, d_{\text{max}})$, given a maximum pairing penalty d_{max} of 10 [72]. Often, the number of predicted CPs does not match the true number N , to which the Hungarian algorithm is employed to find the optimal pairings [86].

For the CPs that are paired, the precision of the inferred location, *i.e.* how close to a true CP is the predicted one, is evaluated by the root mean squared error RMSE_{CP}

^{*} Unlike the definition from [85] which takes vectorised OHE labels of the L classes; our equivalent implementation instead uses a *sparse* CE for integer $t_{\text{loc}}^{\text{CP}}(b_\tau)$ labels, saving some memory and computation time.

[‡] To evaluate TPs in the case of zero CPs in the ground truth (single-state trajectories), the AnDi metrics algorithm counts the correct prediction of no CPs as one TP – the case of a true negative TN, really.

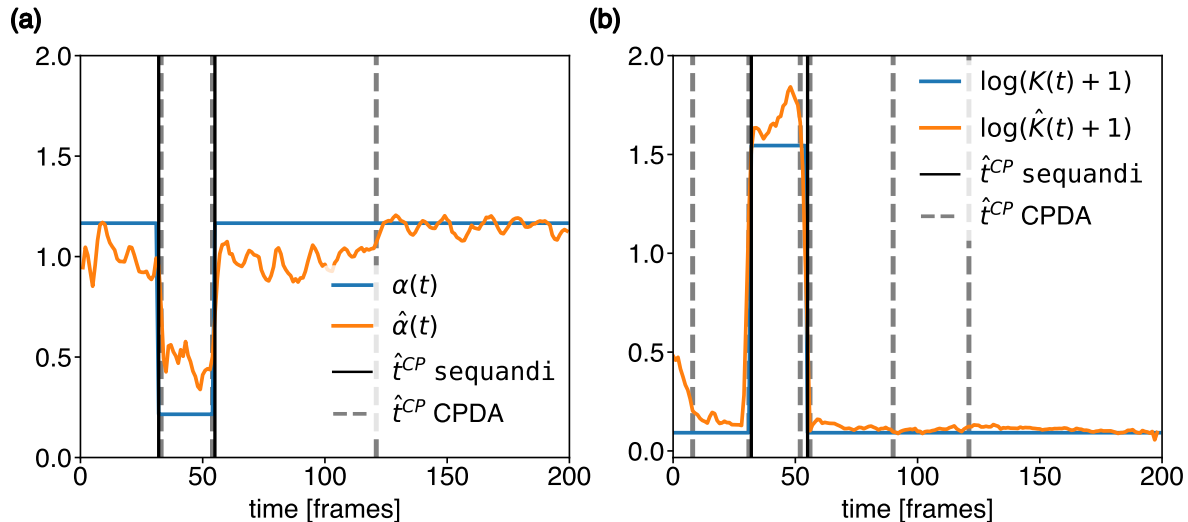


Figure 4. Changepoint detection comparison: sequandi vs. CPDA Using the trajectory illustrated in Fig. 1, the two vertical solid black lines are *sequandi*'s prediction \hat{t}^{CP} . **(a)** As in Fig. 3, the orange line is $\hat{\alpha}(t)$, and the blue piece-wise constant line is the ground truth $\alpha(t)$. The three vertical dashed gray lines are obtained by the CPDA algorithm described in Section 4.4 applied to $\hat{\alpha}(t)$ with a confidence level of 99.99%. **(b)** As in Fig. 3, the orange line is $\log(\hat{K}(t)+1)$ and the blue piece-wise constant line is the ground truth $\log(K(t)+1)$. The six vertical dashed gray lines are obtained by the CPDA algorithm described in Section 4.4 applied to $\log(\hat{K}(t)+1)$ with a confidence level of 99.99%.

metric

$$\text{RMSE}_{\text{CP}} = \sqrt{\frac{1}{N_{\text{TP}}} \sum_{\text{paired } i,j}^{N_{\text{TP}}} (t_i^{\text{CP}} - \hat{t}_j^{\text{CP}})^2}. \quad (9)$$

Importantly, the weight of the mean inside the square root is by the number of TPs N_{TP} that have been found by the algorithm. For a given set of trajectory data, one pools together all of the found TP segments across trajectories to calculate these metrics, as with the FNs and FPs in the JSC_{CP} .

For all the trajectories contained in the benchmark dataset, the detection metrics of *sequandi* are $\text{JSC}_{\text{CP}} = 0.577$ and $\text{RMSE}_{\text{CP}} = 1.504$.

4.4. Detecting a changepoint from the inferred $\hat{\alpha}(t)$ and $\hat{K}(t)$ with an algorithm.

An alternative way of detecting and locating a CP is to exploit the pointwise time-dependent prediction of $\hat{\alpha}(t)$ and $\hat{K}(t)$, and apply a changepoint detection algorithm, as done, for instance, in Ref. [56]. Here, we apply the Changepoint Detection Algorithm (CPDA) developed in Ref. [77] to the time series $\hat{\alpha}(t)$ and $\hat{K}(t)$ obtained in Section 3. The authors of Ref. [77] improved the method proposed in Ref. [87], casting CP detection as a hypothesis testing problem and applied it to analyse the rotary motion of the F₁ molecular motor. The algorithm requires setting a confidence level for accepting the

hypothesis that there was a changepoint, as we discuss in Appendix C. Setting the optimal confidence level requires balancing the trade-off between missing CPs (false negative) and wrongly detecting CPs when there was not one (false positive). The optimal choice depends on the data under consideration as we discuss in Appendix C and Fig.C2. For the benchmark dataset, we find a confidence level of 99.99% returns the best performance in terms of JSC. The CPDA applied to the temporal profile $\hat{\alpha}(t)$ returns consistent results, even though it displays a tendency to detect false positives CPs, as exemplified in Fig.4(a). The $\hat{K}(t)$ profile is less suitable for the CPDA as it accentuates the tendency to return false positives, as shown in Fig.4(b). We, therefore, focus on the performance of the CPDA applied to the $\hat{\alpha}(t)$ profile. The CDPA does not reach the performance of `sequandi` and achieves a $\text{JSC}_{\text{CP}} = 0.2470$ (roughly half of the one of `sequandi`) and $\text{RMSE}_{\text{CP}} = 3.065$ (roughly twice the one of `sequandi`). However, despite its sensitivity to fluctuations in $\hat{\alpha}(t)$ and its tendency to return false positive detections, the CPDA outperforms `sequandi` for trajectories displaying many CPs, as we discuss in Section 5.

5. `sequandi` and the AnDi challenge 2024

In this Section, we describe how the `sequandi` network, which is proficient at capturing the time-dependent point-wise behaviour of the diffusive parameters, performs on the metrics evaluated by AnDi2024.

5.1. Structure of AnDi2024 data and task

In AnDi2024, the goal is to infer the anomalous diffusion exponent α and generalised diffusion coefficient K for each of the N segments, characterised by different diffusive states that may be present in a single trajectory (α_i and K_i for $i = 0, \dots, N - 1$). Also fundamental is the changepoint time t_i^{CP} , *i.e.*, the times at which the system switches between diffusive modes. All together, each trajectory is characterised by the vector containing the list of all the anomalous diffusion exponents, generalised diffusion coefficients and CPs (one per diffusive segment):

$$[\alpha_0, K_0, t_0^{\text{CP}}, \dots, \alpha_i, K_i, t_i^{\text{CP}}, \dots, \alpha_{N-1}, K_{N-1}, T - 1]. \quad (10)$$

In the final, so-called Challenge Phase of AnDi2024, the data was provided in folders of 12 different simulated experiments, each containing trajectories with unique α , K and CPs, drawn from a distribution specific to that experiment, which is chosen from one of the diffusion models described in Section 1.

5.2. Performance metrics of AnDi2024

The pairing of the different diffusive segments is discussed in Section 4.3. In addition to the JSC and the RMSE for CPs, AnDi2024 evaluates the performance of the inference

of α and K . This is evaluated for paired segments as

$$\text{MAE}_\alpha = \frac{1}{N_{TP}} \sum_{\text{paired } i, j}^{N_{TP}} |\alpha_i - \hat{\alpha}_j|, \quad (11)$$

$$\text{MSLE}_K = \frac{1}{N_{TP}} \sum_{\text{paired } i, j}^{N_{TP}} \left[\log [K_i + 1] - \log [\hat{K}_j + 1] \right]^2. \quad (12)$$

This is the error between the ground truths in Eq. (10) and segment-wise predictions $\hat{\alpha}_i, \hat{K}_i$, which we calculate in the next Section. We note that the calculation is over all of the identified TPs in the dataset together.

5.3. Performances of *sequandi* on AnDi2024

Our method, *sequandi*, is designed to return the time-dependent point-wise prediction $\hat{\alpha}(t), \hat{K}(t)$. We therefore need to process the output of *sequandi* to obtain the predictions required by AnDi2024, *i.e.*, the vector of Eq. (10). To this aim, we first divide a trajectory in segments based on the \hat{t}_i^{CP} predicted by the network described in Section 4. We then compute the time average of $\hat{\alpha}(t)$ and $\hat{K}(t)$, within each predicted segment i ,

$$\hat{\alpha}_i = \frac{\sum_{t=\hat{t}_i^{\text{CP}}}^{\hat{t}_{i+1}^{\text{CP}}-1} \hat{\alpha}(t)}{(\hat{t}_{i+1}^{\text{CP}} - 1) - \hat{t}_i^{\text{CP}}}, \quad \hat{K}_i = \frac{\sum_{t=\hat{t}_i^{\text{CP}}}^{\hat{t}_{i+1}^{\text{CP}}-1} \hat{K}(t)}{(\hat{t}_{i+1}^{\text{CP}} - 1) - \hat{t}_i^{\text{CP}}}. \quad (13)$$

Figure 5 shows the segment-wise predictions $\hat{\alpha}_i$ and \hat{K}_i for the trajectory shown in Fig. 1, together with the point-wise predictions $\hat{\alpha}(t)$ and $\hat{K}(t)$ also shown in Fig. 3. In this case, due to accurate predictions \hat{t}_i^{CP} by *sequandi*, the $\hat{\alpha}_i, \hat{K}_i$ are not far from the ground truth. However, in general, inaccuracies in predicting the CPs propagate and amplify, yielding inaccurate $\hat{\alpha}_i$ and \hat{K}_i from what may otherwise have been informative and accurate $\hat{\alpha}(t)$ and $\hat{K}(t)$.

In AnDi2024, *sequandi*, under the KCL team name, finished 8th overall in the Single-trajectory Task. To evaluate the performance in estimating the diffusion parameters, it is instructive to plot the MAE_α vs the MSLE_K as shown in Fig. 6(a). In such a plot, a perfect prediction is located in the left bottom corner [marked by a star in Fig. 6(a)]. The method of Ref. [73] outperforms the other ones, and *sequandi* is close to the cluster of runner-up methods.

For the changepoint detection and location, we plot the JSC vs the RMSE in Fig. 6(b). The optimal prediction in this plot is on the top left corner [marked by a star in Fig. 6(b)]. Also in this task, the best method is the one of Ref. [73] followed by a cluster of 4 runner-up methods. *sequandi* is located after the runner-up cluster.

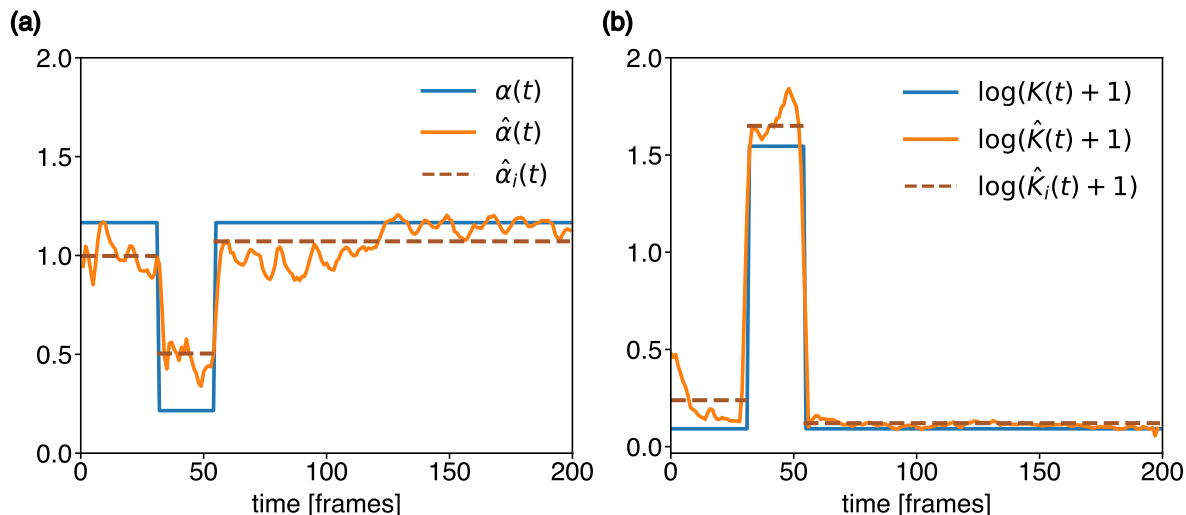


Figure 5. Segmentation of $\hat{\alpha}(t)$ and $\hat{K}(t)$. We segment the trajectory shown in Fig. 1 based on the CPs predicted by `sequandi` \hat{t}^{CP} , which were indicated by the solid black lines shown in Fig. 4. **(a)** As in Fig. 3, the orange line is $\hat{\alpha}(t)$, and the blue piece-wise constant line is the ground truth $\alpha(t)$. The dashed brown line is the time averaged exponent for each segment $\hat{\alpha}_i$, following Eq. (13). **(b)** As in Fig. 3, the orange line is $\log(\hat{K}(t) + 1)$ and the blue piece-wise constant line is the ground truth $\log(K(t) + 1)$. The dashed brown line is based on the time averaged generalised diffusion for each segment \hat{K}_i , following Eq. (13), and is $\log(\hat{K}_i + 1)$.

5.4. Benchmark dataset

To gain further insight into the capabilities of `sequandi`, we took advantage of the AnDi2024 benchmark dataset [79]. This dataset is similar to the 2024 AnDi Challenge one and contains 9 different simulated experiments:

- *Experiment 1*: A 3-state model inspired by the experiments of [88]. All states are characterised by α close to the normal diffusion $\alpha \sim 1$ but each state has a different K , see the x axis of Fig. D1 and D2. Switching between states occurs rapidly.
- *Experiments 2 and 5*: Two dimerisation models. Experiment 2 is inspired by [89], where two particles can bind and unbind, therefore being present in a bound and unbound state of similar $\alpha \sim 1$ but different K . In Experiment 5, one of the states has $\alpha \sim 1$, and the other one is strongly sub-diffusive $\alpha < 0.25$.
- *Experiments 3 and 9*: Two trapping models characterised by a state where there is no motion ($\alpha \sim 0$, $K \sim 0$). Outside of the immobile state, Experiment 3 features diffusion close to normal $\alpha \sim 1$. In Experiment 9, motion is nearly ballistic, with transitions out of the trapped state occurring much more frequently.
- *Experiment 4*: Confinement model with distinct, slow confined state.
- *Experiments 6 and 7*: Dimerisation and 2-state model, respectively. They share identical diffusive parameters, but with different underlying experimental constraints.

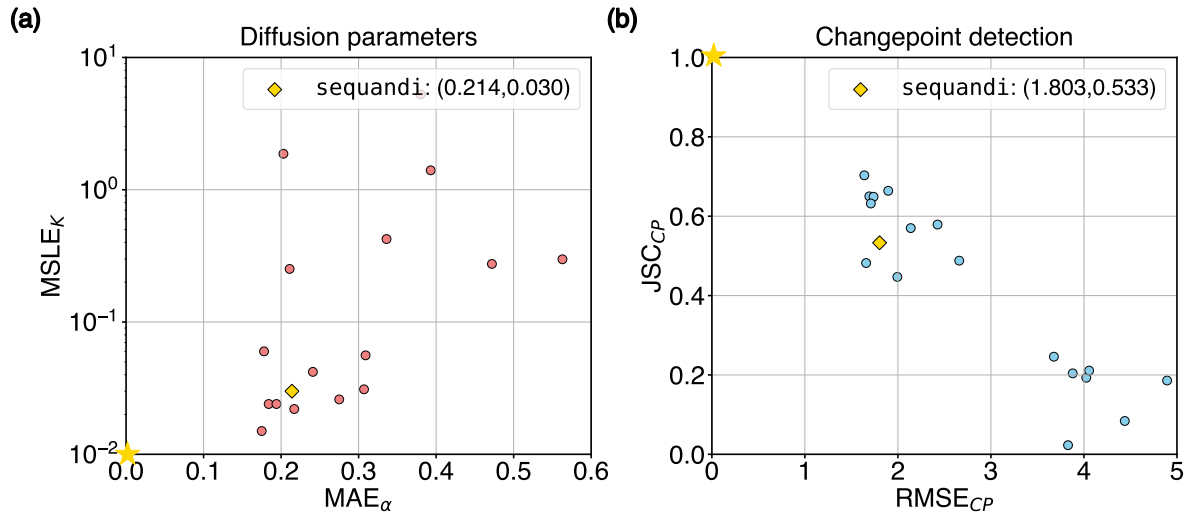


Figure 6. Performance of sequandi in the 2024 AnDi Challenge. (a) For the inference of the diffusion parameters, the $MSLE_K$ is plotted against the MAE_α . The star in the bottom left corner marks the performance of a hypothetical perfect prediction. The circles show the performances of the other methods participating in the 2024 AnDi challenge and the rhombus the one of **sequandi**. (b) For the detection and location of CPs, the JSC_{CP} is plotted against the $RMSE_{CP}$. The star in the top left corner marks the performance of a hypothetical perfect prediction. Again, the circles show the performances of the other methods participating in the challenge and the rhombus the one of **sequandi**.

- *Experiment 8*: Single-state diffusion with broad distributions of α and K .

The distribution of the various diffusive parameters can be seen by observing the ground truth values of the plots in Figs. D1 and D2.

As stated before, **sequandi** is designed to perform a time-dependent, point-wise inference of $\hat{\alpha}(t)$ and $\hat{K}(t)$. This task is, in principle, more difficult than estimating just the diffusive parameters within a segment of a trajectory α_i and K_i . The point-wise metrics $MAE_{\alpha(t)}$, $MSLE_{K(t)}$ are more stringent than the segment-wise MAE_α , $MSLE_K$. However, processing the point-wise output of **sequandi**, $\hat{\alpha}(t)$ and $\hat{K}(t)$, to obtain the segment-wise $\hat{\alpha}_i$ and \hat{K}_i is prone to errors due to the uncertainty in estimating the CPs. As a result, we find that, on the benchmark data, the segment-wise metrics are $MAE_\alpha = 0.206$, $MSLE_K = 0.027\dagger\dagger$, which are significantly worse than the point-wise metrics from the set of flattened $\hat{\alpha}(t)$ and $\hat{K}(t)$ sequences ($MAE_{\alpha(t)} = 0.176$, $MSLE_{K(t)} = 0.014$).

It is interesting to analyse each experiment separately, as reported in Fig. 7.

$\dagger\dagger$ Throughout the paper, the metrics on the benchmark dataset are averages of the metrics obtained on each of the 9 experiments, weighted by the number of trajectories belonging to each experiment. The AnDi2024 segment-wise metrics expressed in Eq. (11) and (12) calculate the error across all of the paired segments in the data together. To make closer contact with this metrics, in this Section, instead of first taking $MAE_{\alpha(t)}$, $MSLE_{K(t)}$ at the trajectory level as in Eq. (4) and (5), we perform the calculation over all of the flattened times t across all the trajectories.

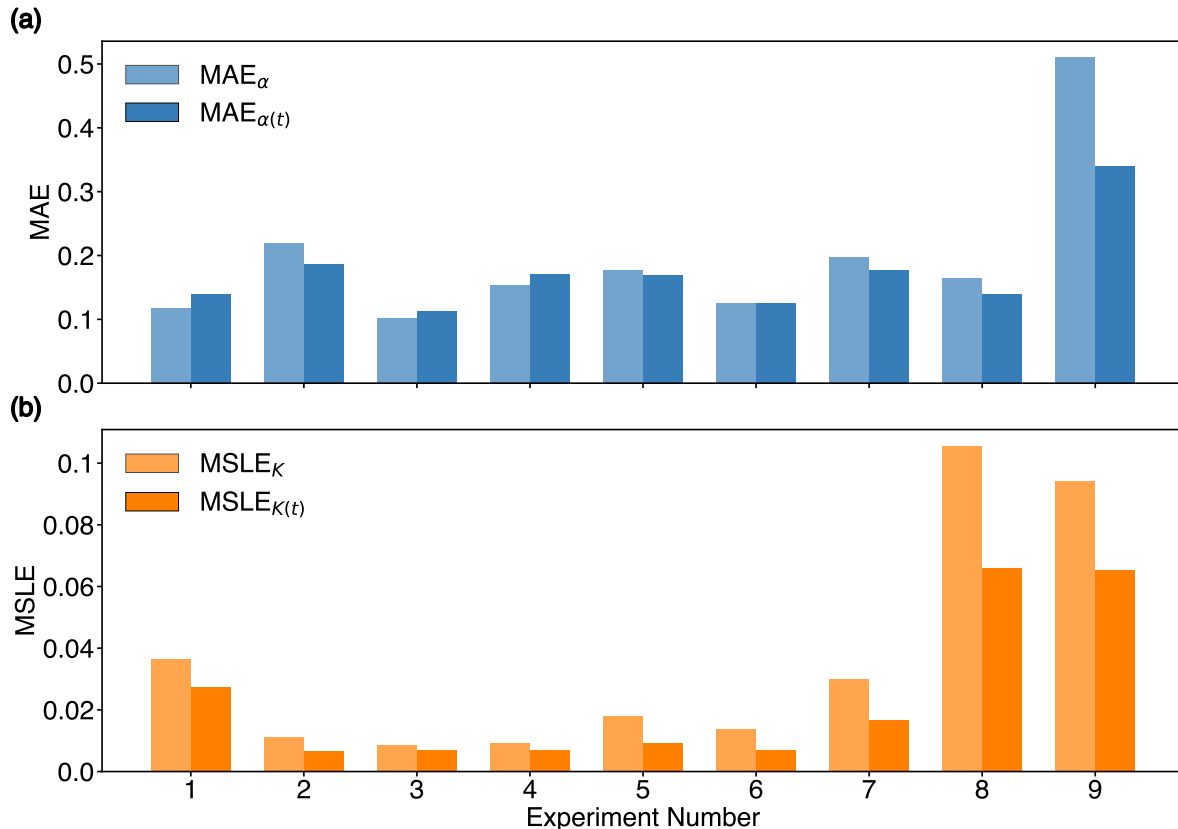


Figure 7. Point-wise (sequandi) and segment-wise performances for diffusion inference on each experiment of the benchmark dataset. (a) Mean absolute error of α per experiment for the segment-wise predictions $\hat{\alpha}_i$, MAE_{α} , and for the point-wise sequential predictions $MAE_{\alpha(t)}$. **(b)** Mean squared logarithmic error (MSLE) of K , per experiment for the segment-wise predictions \hat{K}_i , $MSLE_K$, and for the point-wise sequential predictions $MSLE_{K(t)}$.

Figure 7(b) shows that the generalised diffusion coefficient K is more accurate for the point-wise estimate than for the segment-wise one. The picture is more nuanced for the inference of the anomalous diffusion exponent α , shown in Fig. 7(a). In Experiments 3 and 4, where the CP detection is accurate (see Fig. 8), the segment-wise prediction is more accurate than the point-wise one. Experiment 1 is exceptional because it displays many challenging CP detections, which lead to poor performance by `sequandi`. In this experiment, the segment-wise prediction outperforms the point-wise one, perhaps because the segments had a very similar ground truth $\alpha \sim 1$.

Overall, for the inference of α and K , `sequandi` performs well and evenly throughout different types of experiments with two exceptions. Experiment 9 is the most challenging one because of its unique combination of immobile states and nearly ballistic ones that are edge cases in the training set, see Fig. A1. Experiment 8 is also challenging for the K inference because it displays a single state but covers a vast range of K , which was not optimised during training (Compare Fig. A1 with Fig. D2).

In Figs. D1 and D2, we report how individual $\hat{\alpha}_i$ and \hat{K}_i predictions compare to their ground truths on an experiment-wise basis.

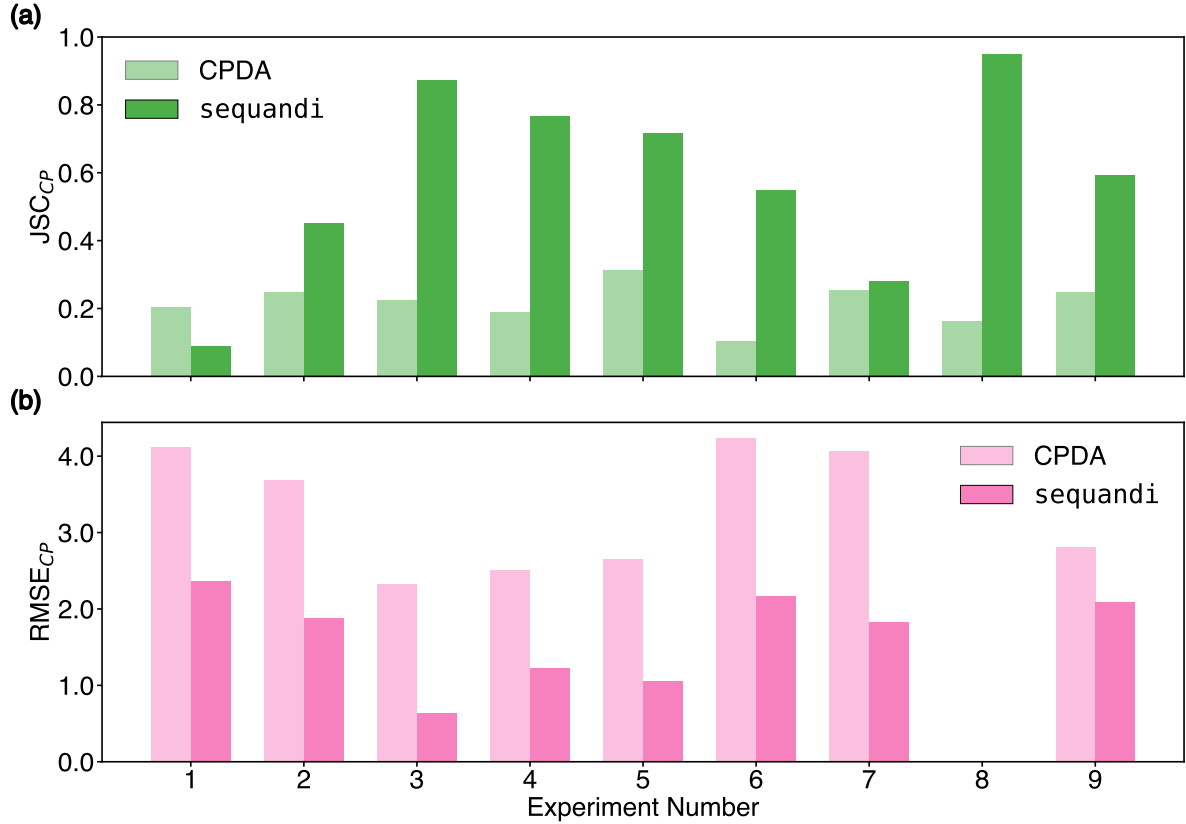


Figure 8. *sequandi* and CPDA performances on CP detection and location on each experiment of the benchmark dataset (a) Comparison of Jaccard Similarity Coefficient of changepoint detections JSC_{CP} , between the CPDA with confidence level 99.99, and by the *sequandi* neural network. $0 \leq JSC \leq 1$, with 1 being perfect detection. (b) Root Mean Squared Error of true positive changepoint detected $RMSE_{CP}$, by *sequandi* and the CPDA.

We now turn our attention to the CP detection and location and the comparison between the predictions of *sequandi* and those of the CPDA, which we report in Fig. 8. As anticipated before, the most challenging CP detections are in Experiment 1, which features frequent transitions between 3 diffusive states, followed by Experiments 2, and 7. *sequandi* systematically outperforms the CPDA applied to $\hat{\alpha}(t)$ except in Experiment 1. The sensitive nature of the CPDA is confirmed by its ability to detect more changepoints than *sequandi* in Experiment 1 and by grossly underperforming in Experiment 8, where there are no CP. We report a detailed analysis of the impact of the confidence levels on the performance of the CPDA in Fig. B1.

6. Conclusion and discussion

This article presents **sequandi**, a method based on LSTM recurrent neural networks to study single trajectories undergoing anomalous diffusion and switching between different diffusive states. Leveraging the properties of RNNs, **sequandi** can analyse trajectories of varying length and returns a point-wise time-dependent estimate of the diffusive properties of the trajectory in terms of its anomalous diffusion exponent α and generalised diffusion coefficient K , $\hat{\alpha}(t)$ and $\hat{K}(t)$, respectively. Such a time-dependent estimate is well-suited to study trajectories that irregularly switch between different diffusive states. We complement this analysis by training another network to detect and locate the changepoints when a switch between different diffusive states occurs \hat{t}^{CP} . We compare the performance of this neural network to that of the Change Point Detection Algorithm (CPDA) proposed in Ref. [77] applied to the time-dependent estimate $\hat{\alpha}(t)$. At variance with the network, the CPDA requires carefully setting a confidence level, which is a non-trivial step, whose optimal solution depends on the task at hand. In general, **sequandi** outperforms the CPDA applied to $\hat{\alpha}(t)$. A possible way to improve the CPDA performance is to apply it to a combination of $\hat{\alpha}(t)$ and $\hat{K}(t)$ or to use also the uncertainty $\sigma_{\alpha}^2(t)$, which one would have to compute, as done in Ref. [55, 56].

We benchmark the performances of **sequandi** on the 2024 Anomalous Diffusion Challenge dataset, which is based on detecting the changepoints and predicting the α and K for each segment between changepoints. This requires combining the results of the network that detects the changepoints \hat{t}_{CP} with the one that infers $\hat{\alpha}(t)$, and $\hat{K}(t)$ and then taking an average over the identified segments. This procedure is not error-free and degrades the performances of the method.

Our study underscores the inherent challenge in integrating algorithmic and neural network-based approaches without propagating errors. This highlights that, when possible, performing the whole analysis with a neural network is advantageous. This is because the network automatically learns ways of compensating uncertainties and errors to return optimal predictions, as shown, for instance, in Ref. [57].

Nonetheless, we stress that the point-wise inferences $\hat{\alpha}(t)$ and $\hat{K}(t)$ of **sequandi** are accurate across a broad scope of systems with switching diffusive behaviour.

Acknowledgements

SB wishes to thank Chun-Biu Li for discussions on the changepoint algorithm of Ref. [77]. XQ was financially supported by the China Scholarship Council through the King’s-China Scholarship Council PhD Scholarship programme (K-CSC).

Appendix A. Training Dataset

In this Appendix, we provide additional details about the structure of the 2.5×10^6 trajectories that we used for training **sequandi**. To generate the training set, we first

uniformly sampled α and $\log K$ and generated the trajectories associated with these values. We then added trajectories with α close to 0 and 1 and small K to have more training data for the most challenging cases. The resulting distributions are shown in Fig. A1 together with the corresponding segment-wise predictions

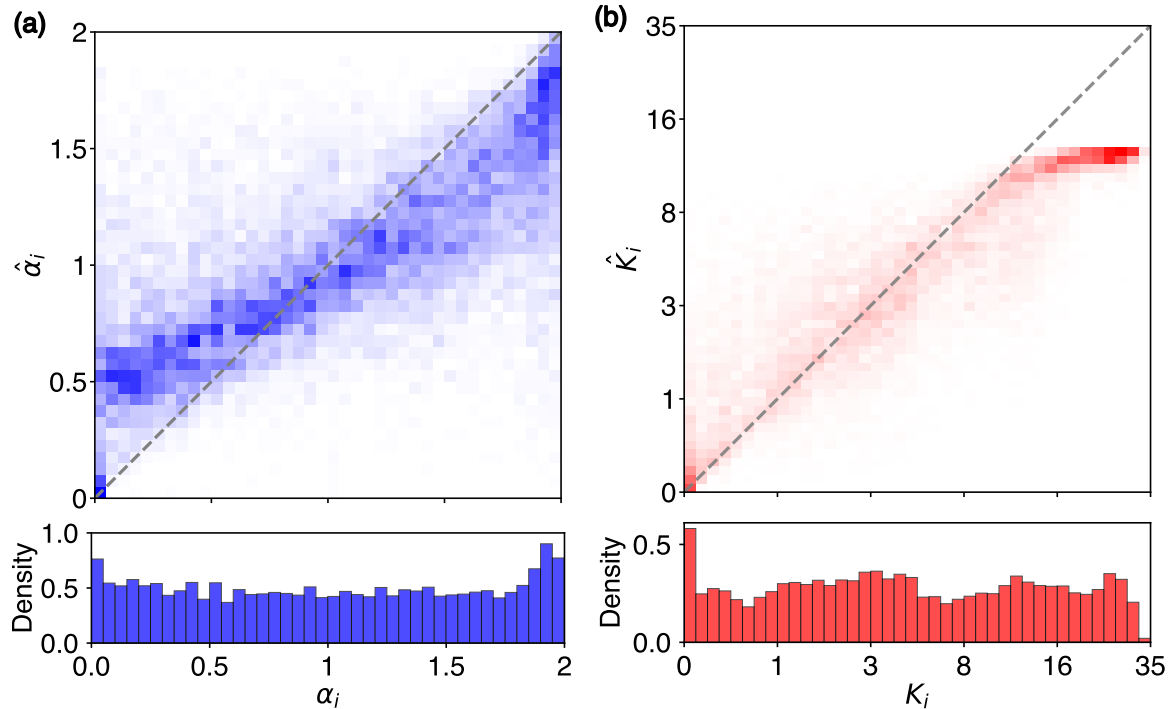


Figure A1. Training trajectory dataset distributions and predictions. (a) Predicted segment-wise anomalous diffusion exponent $\hat{\alpha}_i$ vs the ground truth α_i for the training dataset of `sequandi`. (b) Predicted segment-wise generalised diffusion coefficient \hat{K}_i vs the ground truth K_i . The bottom row of histograms show the distribution of the ground truth parameters of the dataset. Note the logarithmic scaling of K .

Appendix B. Neural network changepoint detection signal

Figure B1 shows an example of the pooled outputs from the two layers of the neural network devoted to detecting and locating changepoints for the trajectory shown in Fig. 1. As described in 4.2, we pool outputs from the neural network’s changepoint detection predictions to compose a signal $\hat{t}^{\text{CP}}(t)$. The final changepoint predictions are extracted from this by finding the peaks of the signal above a threshold count of 2 (dashed gray line) and with a minimum time 3 between them.

Appendix C. Changepoint algorithm optimisation

In this Appendix, we provide additional details about our implementation of the CPDA developed in Ref. [77]. The algorithm consists of three main steps: detecting the pres-

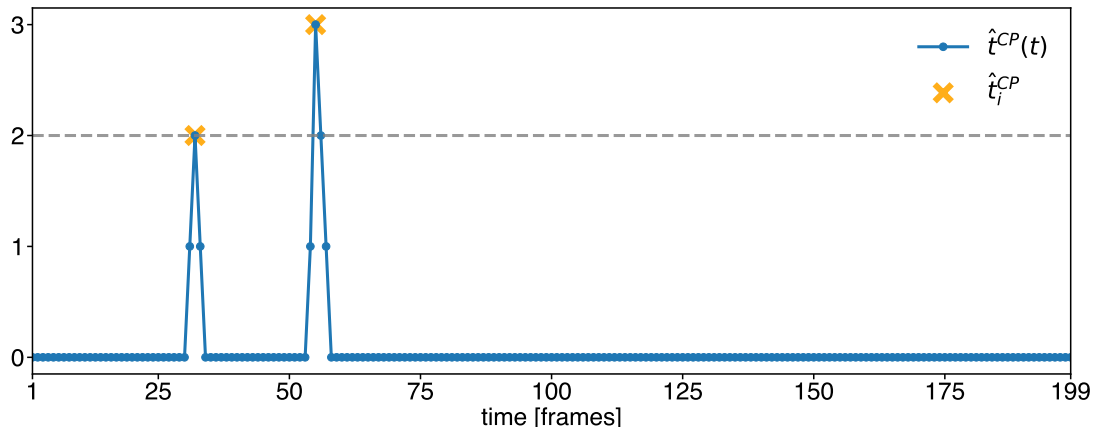


Figure B1. Changepoint Detection from pooled neural network signal. Pooled outputs of the two parallel layers of the neural network detecting and locating changepoints for the example trajectory shown in Fig 1.

ence of a CP, locating the CP and dealing with multiple CPs.

- *Step 1: Detecting a changepoint*

The first step checks if there are changepoints in a trajectory segment. Here, we are using as input the prediction from our networks $\hat{\alpha}(t)$. A straight line $\alpha_{\text{fit}}(t)$ is fitted. The residual is computed as $d(t) = \hat{\alpha}(t) - \alpha_{\text{fit}}(t)$, followed by the cumulative sum $\text{CUMSUM}(t)$ of $d(t)$. The statistic D_{data} is the difference between the maximum and minimum values of $\text{CUMSUM}(t)$. The significance of D_{data} is tested by permuting $d(t)$ multiple times to generate a distribution of $\text{CUMSUM}(t)$ curves and D_{permute} values. A confidence level (e.g., 95%) sets the threshold D_{cutoff} . If $D_{\text{data}} \geq D_{\text{cutoff}}$, a changepoint is present. We discuss the relevance of the confidence level in Appendix C.1

- *Step 2: Locating the changepoint*

After confirming a changepoint, its position is found by testing each point t in the trajectory. For each t , the segments before and after are fitted with straight lines, and the squared error (SE) is calculated as the sum of squared residuals. The t with the smallest SE is the changepoint.

- *Step 3: Locating Multiple changepoints*

To find multiple changepoints, the trajectory is split at each detected changepoint, and Steps 1 and 2 are repeated on each segment until no further changepoints are found.

Each changepoint \hat{t}_i^{CP} is then validated by re-analysing the segment from $\hat{t}_{i-1}^{\text{CP}}$ to \hat{t}_i^{CP} , applying Step 1's hypothesis test and Step 2's localisation to confirm its robustness.

Appendix C.1. Confidence levels for the CPDA

The CPDA requires choosing the confidence level to make the decision about whether a CP is present in a segment. This is a crucial parameter determining the sensitivity of the changepoint detection. Setting the confidence too low results in many false positives (claiming a CP occurred when it did not), and setting it too high in many false negatives (missing CP that occurred).

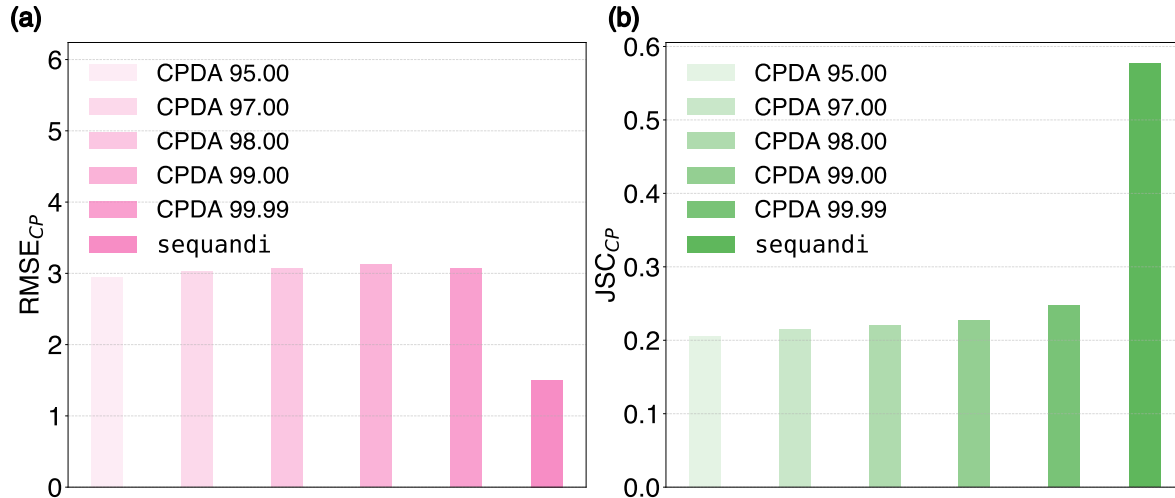


Figure C1. Comparison of CPDA and sequandi Performance. The confidence levels used are from Appendix C.1. (a) shows the RMSE of different confidence levels for CPDA and Sequandi, while (b) presents the JSC performance under the same settings. Lower RMSE and higher JSC values indicate better performance.

For the AnDi 2 Benchmark dataset, we explore confidence levels of 95%, 97%, 98%, 99%, and 99.99%, with a permutation number of 10,000. The ability of the CPDA to detect CPs increases with the confidence level, as shown in Fig. C1(b). The precision of the detected CPs, quantified by the RMSE in Eq. (9), exhibits a non-monotonic trend, initially increasing before decreasing, as shown in Fig. C1(a).

It is interesting to consider the performance of the CPDA on each of the experiments of AnDi2024, which we report in Fig. C2. As expected, we see that a higher confidence level reduces the number of false positives [Fig. C2(b)] but increases the number of false negatives [Fig. C2(c)]. The behaviour of the true positives [Fig. C2(a)] shows the opposite trend, with the exception of Experiment 3. The JSC of the algorithm display a more intricate behaviour, which depends on the experiment. For Experiments 1 and 9, which feature many changepoints, a low confidence interval returns the best JSC. For Experiments 2 and 7, there is an intermediate optimal confidence level. In the remaining experiments, which do not feature many changepoints, a high confidence level gives the best JSC.

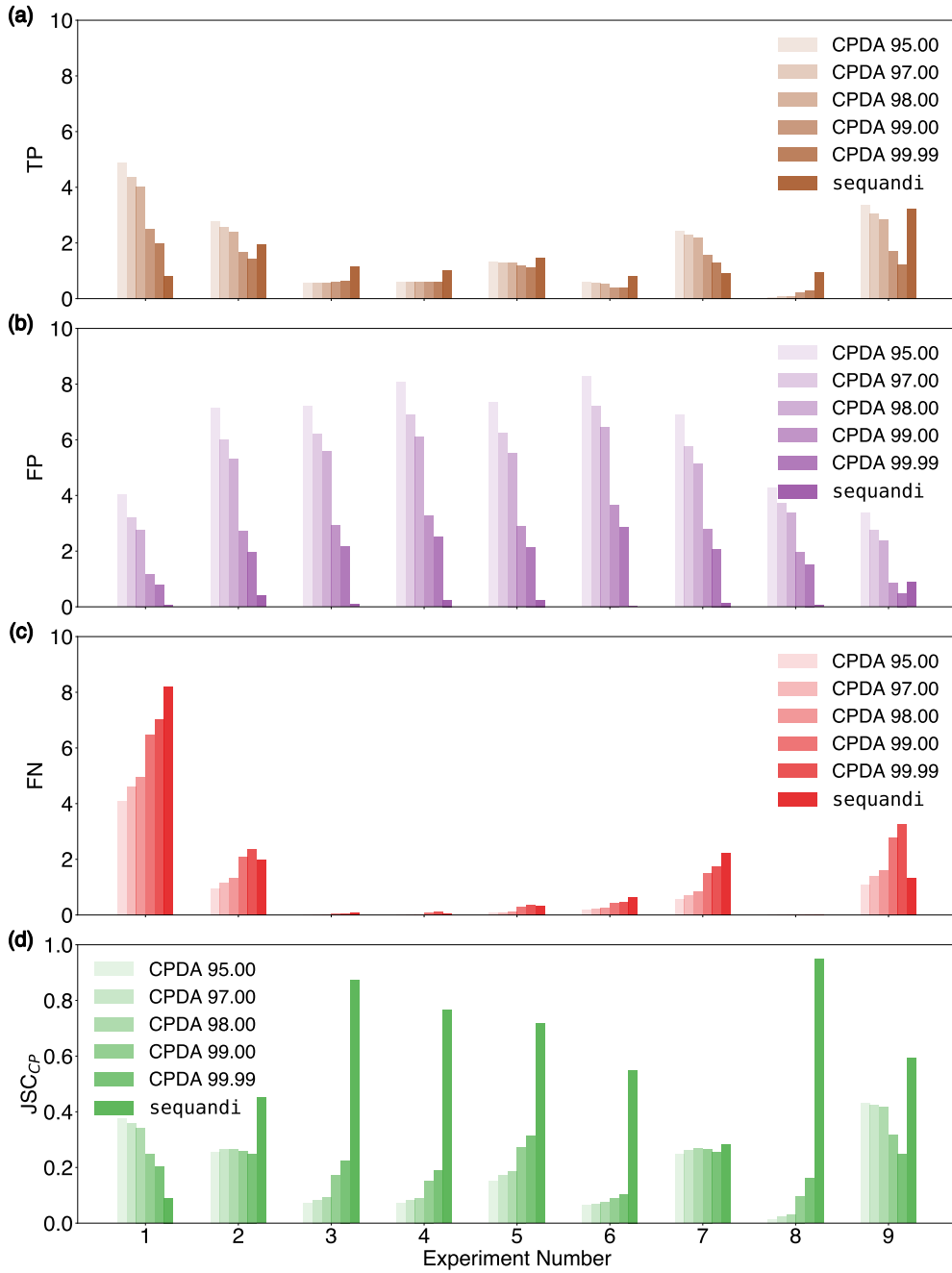


Figure C2. Comparison of CPDA and sequandi for each experiment (a) True positives (TP) of the changepoint detection normalised by the number of trajectories for each experiment in the benchmark dataset and different confidence levels of the CPDA. (b) False positives (FP) of the changepoint detection normalised by the number of trajectories for each experiment in the benchmark dataset and different confidence levels of the CPDA. (c) False negatives (FN) of the changepoint detection normalised by the number of trajectories for each experiment in the benchmark dataset and different confidence levels of the CPDA. (d) JSC for each experiment in the benchmark dataset and different confidence levels of the CPDA

Appendix D. Benchmark dataset experiment-wise performance

In this appendix we report the performance of the segment-wise predictions on the benchmark dataset discussed in Section 5.4 for each experiment.

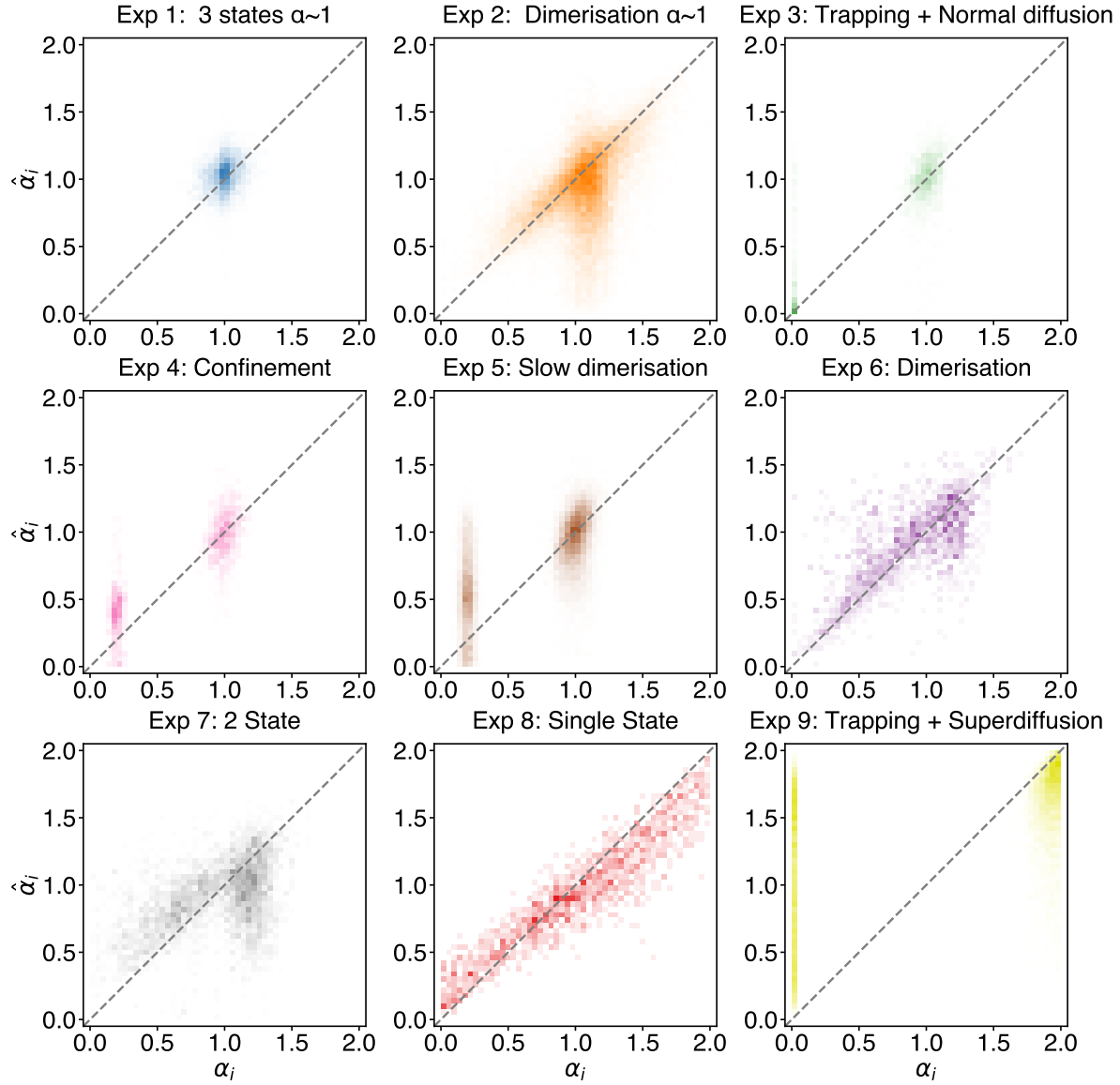


Figure D1. Ground truth vs. predicted anomalous diffusion exponent. For each experiment in the benchmark dataset, a heat-map of the predicted segment-wise $\hat{\alpha}_i$ and their respective ground truths.

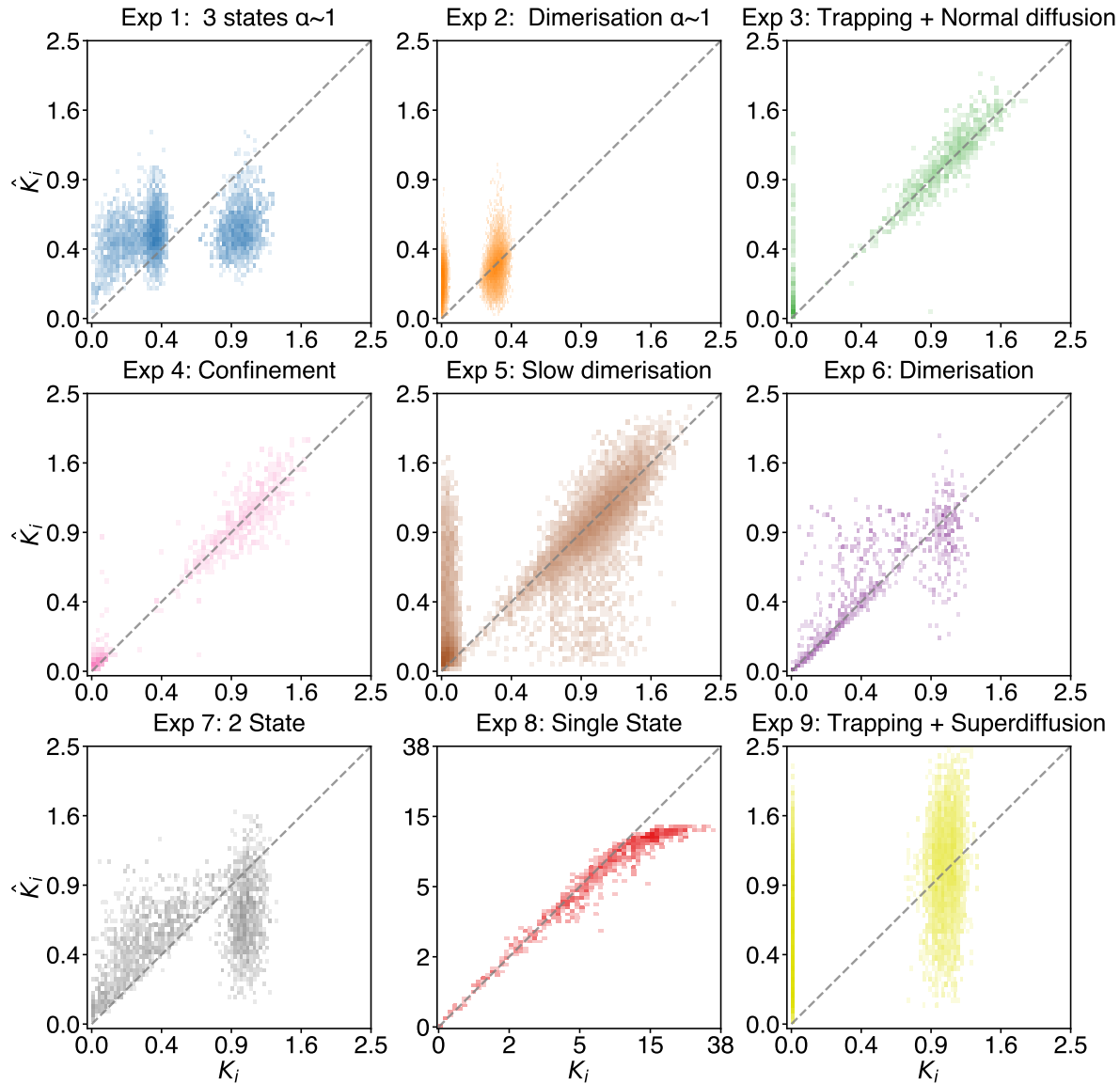


Figure D2. Ground truth vs. predicted generalised diffusion coefficient. For each experiment in the benchmark dataset, a heat-map of the predicted segment-wise \hat{K}_i and their respective ground truths. The x and y axis scales are logarithmic, and the colourisation of the heat-map is with a logarithmic normalisation due to the more dilute grid.

References

- [1] Phillips R, Kondev J, Theriot J, Orme N and Garcia H 2009 *Physical biology of the cell* (Garland Science New York)
- [2] Einstein A 1905 *Annalen der physik* **4**
- [3] Cohen L 2005 *IEEE Signal Processing Magazine* **22** 20–45

- [4] Gardiner C W 1985 *Handbook of stochastic methods for physics, chemistry and the natural sciences* (Springer Berlin Heidelberg)
- [5] Klafter J and Sokolov I M 2011 *First steps in random walks: from tools to applications* (OUP Oxford)
- [6] Aghion E, Meyer P G, Adlakha V, Kantz H and Bassler K E 2021 *New Journal of Physics* **23** 023002
- [7] Vilk O, Aghion E, Avgar T, Beta C, Nagel O, Sabri A, Sarfati R, Schwartz D K, Weiss M, Krapf D *et al.* 2022 *Physical Review Research* **4** 033055
- [8] Squires T M and Mason T G 2010 *Annual review of fluid mechanics* **42** 413–438
- [9] Brown R 1828 *The philosophical magazine* **4** 161–173
- [10] Jones P H, Maragò O M and Volpe G 2015 *Optical Tweezers: Principles and Applications* (Cambridge University Press)
- [11] Argun A, Callegari A and Volpe G 2021 *Simulation of Complex Systems* (IOP Publishing)
- [12] Chen L, Bassler K E, McCauley J L and Gunaratne G H 2017 *Physical Review E* **95** 042141
- [13] Meyer P G, Aghion E and Kantz H 2022 *Journal of Physics A: Mathematical and Theoretical* **55** 274001
- [14] Mandelbrot B B and Wallis J R 1968 *Water resources research* **4** 909–918
- [15] Klafter J and Sokolov I M 2005 Anomalous diffusion spreads its wings URL <https://iopscience.iop.org/article/10.1088/2058-7058/18/8/33>
<https://iopscience.iop.org/article/10.1088/2058-7058/18/8/33/meta>
- [16] Barkai E, Garini Y and Metzler R 2012 *Physics Today* **65** 29–35 ISSN 00319228 URL <http://physicstoday.scitation.org/doi/10.1063/PT.3.1677>
- [17] Höfling F and Franosch T 2013 *Reports on Progress in Physics* **76** 046602 ISSN 00344885 (*Preprint* 1301.6990) URL <http://stacks.iop.org/0034-4885/76/i=4/a=046602?key=crossref.d72b9b76244e9222284e073065248855>
- [18] Metzler R, Jeon J H, Cherstvy A G and Barkai E 2014 *Physical Chemistry Chemical Physics* **16** 24128–24164 ISSN 14639076 URL <http://xlink.rsc.org/?DOI=C4CP03465A>
- [19] Lucas J S, Zhang Y, Dudko O K and Murre C 2014 *Cell* **158** 339–352
- [20] Zhang Y and Dudko O K 2016 *Annual review of biophysics* **45** 117–134
- [21] Khanna N, Zhang Y, Lucas J S, Dudko O K and Murre C 2019 *Nature communications* **10** 2771
- [22] Gabriele M, Brandão H B, Grosse-Holz S, Jha A, Dailey G M, Cattoglio C, Hsieh T H S, Mirny L, Zechner C and Hansen A S 2022 *Science* **376** 496–501
- [23] Yesbolatova A K, Arai R, Sakaue T and Kimura A 2022 *Physical Review Letters* **128** 178101

- [24] Jeon J H and Metzler R 2010 *Journal of Physics A: Mathematical and Theoretical* **43** ISSN 17518113
- [25] Golding I and Cox E C 2006 *Physical Review Letters* **96** 14–17 ISSN 00319007
- [26] Bronstein I, Israel Y, Kepten E, Mai S, Shav-Tal Y, Barkai E and Garini Y 2009 *Physical Review Letters* **103** 018102 ISSN 00319007 URL <https://link.aps.org/doi/10.1103/PhysRevLett.103.018102>
- [27] Weber S C, Spakowitz A J and Theriot J A 2010 *Physical Review Letters* **104** 27–30 ISSN 00319007
- [28] Jeon J H, Leijnse N, Oddershede L B and Metzler R 2013 *New Journal of Physics* **15** 045011 ISSN 13672630 URL <http://stacks.iop.org/1367-2630/15/i=4/a=045011?key=crossref.736240d80ee0c7c1a33d6c582cfce278>
- [29] Caspi A, Granek R and Elbaum M 2000 *Physical Review Letters* **85** 5655–5658 ISSN 10797114 URL <https://link.aps.org/doi/10.1103/PhysRevLett.85.5655>
- [30] Tejedor V, Bénichou O, Voituriez R, Jungmann R, Simmel F, Selhuber-Unkel C, Oddershede L B and Metzler R 2010 *Biophysical Journal* **98** 1364–1372 ISSN 15420086
- [31] Burnecki K, Kepten E, Garini Y, Sikora G and Weron A 2015 *Scientific Reports* **5** 1–11 ISSN 20452322 URL <http://dx.doi.org/10.1038/srep11306>
- [32] Meroz Y and Sokolov I M 2015 *Physics Reports* **573** 1–29 ISSN 03701573 URL <https://www.sciencedirect.com/science/article/pii/S0370157315001404>
- [33] Makarava N, Benmehdi S and Holschneider M 2011 *Physical Review E - Statistical, Nonlinear, and Soft Matter Physics* **84** 021109 ISSN 15393755 URL <https://link.aps.org/doi/10.1103/PhysRevE.84.021109>
- [34] Hinsén K and Kneller G R 2016 *Journal of Chemical Physics* **145** 151101 ISSN 00219606 URL <http://aip.scitation.org/doi/10.1063/1.4965881>
- [35] Weron A, Janczura J, Boryczka E, Sungkaworn T and Calebiro D 2019 *Physical Review E* **99** 042149 ISSN 24700053 URL <https://link.aps.org/doi/10.1103/PhysRevE.99.042149>
- [36] Elf J and Barkefors I 2019 *Annual Review of Biochemistry* **88** 635–659 ISSN 15454509 (*Preprint* 1809.03265) URL <https://www.annualreviews.org/doi/10.1146/annurev-biochem-013118-110801>
- [37] Akin E J, Solé L, Johnson B, el Beheiry M, Masson J B, Krapf D and Tamkun M M 2016 *Biophysical Journal* **111** 1235–1247 ISSN 15420086
- [38] Sikora G, Wyłomańska A, Gajda J, Solé L, Akin E J, Tamkun M M and Krapf D 2017 *Physical Review E* **96** 062404 ISSN 24700053 URL <https://link.aps.org/doi/10.1103/PhysRevE.96.062404>
- [39] Weron A, Burnecki K, Akin E J, Solé L, Balcerek M, Tamkun M M and Krapf D 2017 *Scientific Reports* **7** 5404 ISSN 20452322 URL <http://www.nature.com/articles/s41598-017-05911-y>

- [40] Krapf D, Lukat N, Marinari E, Metzler R, Oshanin G, Selhuber-Unkel C, Squarcini A, Stadler L, Weiss M and Xu X 2019 *Physical Review X* **9** 011019 ISSN 21603308 URL <https://link.aps.org/doi/10.1103/PhysRevX.9.011019>
- [41] Vilk O, Aghion E, Nathan R, Toledo S, Metzler R and Assaf M 2022 *Journal of Physics A: Mathematical and Theoretical* **55** 334004
- [42] Kepten E, Bronshtein I and Garini Y 2013 *Physical Review E - Statistical, Nonlinear, and Soft Matter Physics* **87** 1–10 ISSN 15393755 (*Preprint* 1212.0793)
- [43] Kepten E, Weron A, Sikora G, Burnecki K and Garini Y 2015 *PLoS ONE* **10** 1–10 ISSN 19326203
- [44] Lanoiselée Y, Sikora G, Grzesiek A, Grebenkov D S and Wyłomańska A 2018 *Physical Review E* **98** 062139 ISSN 24700053 URL <https://link.aps.org/doi/10.1103/PhysRevE.98.062139>
- [45] Wagner T, Kroll A, Haramagatti C R, Lipinski H G and Wiemann M 2017 *PLoS ONE* **12** e0170165 ISSN 19326203 URL <https://dx.plos.org/10.1371/journal.pone.0170165>
- [46] Bo S, Schmidt F, Eichhorn R and Volpe G 2019 *Physical Review E* **100** ISSN 24700053 (*Preprint* 1905.02038)
- [47] Muñoz-Gil G, Garcia-March M A, Manzo C, Martín-Guerrero J D and Lewenstein M 2020 *New Journal of Physics* **22** 013010 ISSN 13672630 URL <https://doi.org/10.1088/1367-2630/ab6065>
- [48] Granik N, Weiss L E, Nehme E, Levin M, Chein M, Perlson E, Roichman Y and Shechtman Y 2019 *Biophysical Journal* **117** 185–192 ISSN 15420086
- [49] Jamali V, Hargus C, Ben-Moshe A, Aghazadeh A, Ha H D, Mandadapu K K and Alivisatos A P 2021 *Proceedings of the National Academy of Sciences* **118** ISSN 0027-8424 URL <https://www.pnas.org/content/118/10/e2017616118>
- [50] Janczura J, Kowalek P, Loch-Olszewska H, Szwabiński J and Weron A 2020 *Physical Review E* **102** 1–25 ISSN 24700053 (*Preprint* 2005.06239)
- [51] Kowalek P, Loch-Olszewska H and Szwabiński J 2019 *Physical Review E* **100** ISSN 24700053 (*Preprint* 1902.07942) URL <http://arxiv.org/abs/1902.07942>
- [52] Loch-Olszewska H and Szwabiński J 2020 *Entropy* **22** 1–25 ISSN 10994300
- [53] Han D, Korabel N, Chen R, Johnston M, Gavrilova A, Allan V J, Fedotov S and Waigh T A 2020 *eLife* **9** 1–28 ISSN 2050084X
- [54] Gentili A and Volpe G 2021 *arXiv (Preprint* 2102.07605) URL <http://arxiv.org/abs/2102.07605>
- [55] Seckler H and Metzler R 2022 *Nature Communications* **13** 6717
- [56] Seckler H and Metzler R 2024 *Journal of Physics: Photonics* **6** 045025
- [57] Argun A, Volpe G and Bo S 2021 *Journal of Physics A: Mathematical and Theoretical* **54** 294003 ISSN 1751-8121 URL <http://dx.doi.org/10.1088/1751-8121/ac070a>

- [58] Pacheco-Pozo A and Krapf D 2024 *Nature Computational Science* **4** 731–732
- [59] Verdier H, Duval M, Laurent F, Cassé A, Vestergaard C L and Masson J B 2021 *Journal of Physics A: Mathematical and Theoretical* **54** 234001
- [60] Qu X, Hu Y, Cai W, Xu Y, Ke H, Zhu G and Huang Z 2024 *Physical Review Research* **6** 013054
- [61] Cai W, Hu Y, Qu X, Zhao H, Wang G, Li J and Huang Z 2024 *arXiv preprint arXiv:2412.01393*
- [62] Zhang Y, Zhu J, Xie H and He Y 2025 *Proceedings of the National Academy of Sciences* **122** e2418643122
- [63] Requena B, Masó-Oriols S, Bertran J, Lewenstein M, Manzo C and Muñoz-Gil G 2023 *Biophysical journal* **122** 4360–4369
- [64] Muñoz-Gil G, i Corominas G G and Lewenstein M 2021 *Journal of Physics A: Mathematical and Theoretical* **54** 504001
- [65] Pineda J, Midtvedt B, Bachimanchi H, Noé S, Midtvedt D, Volpe G and Manzo C 2023 *Nature Machine Intelligence* **5** 71–82
- [66] Seckler H, Szwabinski J and Metzler R 2023 *The journal of physical chemistry letters* **14** 7910–7923
- [67] Garibo-i Orts Ò, Baeza-Bosca A, Garcia-March M A and Conejero J A 2021 *Journal of Physics A: Mathematical and Theoretical* **54** 504002 URL <https://dx.doi.org/10.1088/1751-8121/ac3707>
- [68] Szarek D 2021 *International Journal of Advances in Engineering Sciences and Applied Mathematics* **13**
- [69] Kabbech H and Smal I 2024 *Journal of Open Source Software* **9** 6157 URL <https://doi.org/10.21105/joss.06157>
- [70] Fernández-Fernández G, Manzo C, Lewenstein M, Dauphin A and Muñoz-Gil G 2024 *Physical Review E* **110** L012102
- [71] Muñoz-Gil G, Volpe G, Garcia-March M A, Aghion E, Argun A, Hong C B, Bland T, Bo S, Conejero J A, Firbas N *et al.* 2021 *Nature communications* **12** 6253
- [72] Muñoz-Gil G, Bachimanchi H, Pineda J, Midtvedt B, Lewenstein M, Metzler R, Krapf D, Volpe G and Manzo C 2024 Quantitative evaluation of methods to analyze motion changes in single-particle experiments (*Preprint* 2311.18100) URL <https://arxiv.org/abs/2311.18100>
- [73] Asghar S, Ni R and Volpe G 2025 U-net 3+ for anomalous diffusion analysis enhanced with mixture estimates (u-and-me) in particle-tracking data (*Preprint* 2502.19253) URL <https://arxiv.org/abs/2502.19253>
- [74] Argun A, Thalheim T, Bo S, Cichos F and Volpe G 2020 *Applied Physics Reviews* **7** 041404 ISSN 19319401 (*Preprint* 2006.08963) URL <http://aip.scitation.org/doi/10.1063/5.0019105>

- [75] Lipton Z C, Berkowitz J and Elkan C 2015 *arXiv (Preprint 1506.00019)* URL <http://arxiv.org/abs/1506.00019>
- [76] Hochreiter S and Schmidhuber J 1997 *Neural Computation* **9** 1735–1780 ISSN 08997667 (*Preprint 1206.2944*)
- [77] Li C B, Ueno H, Watanabe R, Noji H and Komatsuzaki T 2015 *Nature communications* **6** 10223
- [78] Lanza A, Qu X and Bo S sequandi URL <https://github.com/bo-lab-kcl/Sequ-AnDi>
- [79] Muñoz-Gil G, Bachimanchi H, Pineda J, Midtvedt B, Requena B, Fernández Fernández G, Lewenstein M, Metzler R, Krapf D, Volpe G and Manzo C 2024 Andi 2 benchmark dataset URL <https://doi.org/10.5281/zenodo.14281479>
- [80] Lipton Z C, Kale D C, Elkan C and Wetzel R 2016 *4th International Conference on Learning Representations, ICLR 2016 - Conference Track Proceedings (Preprint 1511.03677)* URL <http://arxiv.org/abs/1511.03677>
- [81] Chollet F and Others 2015 Keras \url{https://keras.io}
- [82] Muñoz-Gil G, Volpe G, Garcia-March M A, Metzler R, Lewenstein M and Manzo C 2021 The anomalous diffusion challenge dataset URL https://github.com/AnDiChallenge/ANDI_datasets
- [83] Gal Y and Ghahramani Z 2016 *Advances in Neural Information Processing Systems* 1027–1035 ISSN 10495258 (*Preprint 1512.05287*)
- [84] Kingma D P and Ba J L 2015 Adam: A method for stochastic optimization *3rd International Conference on Learning Representations, ICLR 2015 - Conference Track Proceedings (International Conference on Learning Representations, ICLR) (Preprint 1412.6980)* URL <https://arxiv.org/abs/1412.6980v9>
- [85] Hart J Keras Ordinal Categorical Crossentropy Loss Function URL https://github.com/JHart96/keras_ordinal_categorical_crossentropy
- [86] Crouse D F 2016 *IEEE Transactions on Aerospace and Electronic Systems* **52** 1679–1696
- [87] Taylor W A 2000 Change-point analysis: a powerful new tool for detecting changes
- [88] Sungkaworn T, Jobin M l, Burnecki K, Weron A, Lohse M and Calebiro D 2017 *Nature* **550**
- [89] Low-Nam S, Lidke K, Cutler P, Roovers R, Bergen en Henegouwen P M, Wilson B and Lidke D 2011 *Nature structural & molecular biology* **18** 1244–9